Stoichiometric and off-stoichiometric full Heusler $Fe_2V_{1-x}W_xAl$ thermoelectric systems

B. Hinterleitner,[1,2] P. Fuchs,[1] J. Rehak,[1] F. Garmroudi,[1] M. Parzer,[1] M. Waas,[1] R. Svagera,[1] S. Steiner,[1,3] M. Kishimoto,[4] R. Moser,[5] R. Podloucky,[5] and E. Bauer[1,2]

[1]*Institute of Solid State Physics, Technische Universität Wien, A-1040 Wien, Austria*
[2]*Christian Doppler Laboratory for Thermoelectricity, Technische Universität Wien, A-1040 Wien, Austria*
[3]*Central European Institute of Technology, Brno University of Technology, Purkynova 123, 61200 Brno, Czech Republic*
[4]*Department of Physics, Tokyo Metropolitan University, Tokyo 192-0397, Japan*
[5]*Institute of Physical Chemistry, Universität Wien, A-1090 Vienna, Austria*

(Received 21 August 2019; revised 2 July 2020; accepted 17 July 2020; published 13 August 2020)

A series of full Heusler alloys, $Fe_2V_{1-x}W_xAl$, $0 \leqslant x \leqslant 0.2$, was prepared and characterized, and relevant physical properties to account for the thermoelectric performance were studied in a wide temperature range. Additionally, off-stoichiometric samples with similar compositions have been included, and a 10% improvement of the thermoelectric figure of merit was obtained. The V/W substitution causes (i) a change of the main carrier type, from holes to electrons as evidenced from Seebeck and Hall measurements, and (ii) a substantial reduction of the lattice thermal conductivity due to a creation of lattice disorder by means of a distinct different mass and metallic radius upon the V/W substitution. Moreover ZT values above 0.2 have been obtained. A microscopic understanding of the experimental data observed is revealed from *ab initio* calculations of the electronic and phononic structure. This series of alloys constitutes the basis for thin film systems, which have recently been found to exhibit ZT values beyond those reported so far in the literature.

DOI: 10.1103/PhysRevB.102.075117

I. INTRODUCTION

Half Heusler XYZ and full Heusler systems X_2YZ have attracted growing interest in many functional materials related fields, such as in spintronics, optoelectronics, superconductivity, shape memory, or thermoelectricity. For the latter, a variety of promising properties such as the mechanical and chemical stability and for several members of XYZ systems a thermoelectric performance with good prospects have been found. Here, X and Y are in general transition metal elements and Z is a main group element such as aluminium. While XYZ systems consist of 3 fcc sublattices, X_2YZ systems are composed of four fcc sublattices. Since Heusler systems are prone to antisite occupations, the cubic crystal structures might change with respect to their space groups and fcc based crystals might transform to bcc type materials. Recent reviews summarize many of the above indicted aspects [1–3].

Full Heusler compounds are known for their closeness to an insulating state, i.e., the proximity of the Fermi energy to a gap in the electronic density of states (eDOS). Specifically, the Fermi energy E_F of Fe_2VAl is located very slightly below a pseudogap in the eDOS (see, e.g., Ref. [4]). Consequently, holes are the main charge carriers and positive Seebeck and Hall values can be obtained experimentally [5]. Small changes of the electron concentration by electron or hole doping is expected to shift E_F either toward the conduction band or more deeply into the valence band, resulting in electron or hole dominated transport, as one of the prerequisites of thermoelectric materials.

Fe_2VAl offers the possibility to exchange elements on all lattice sites, i.e., on the Fe site (8c), on the V site (4a), and on the Al site (4b) of the Cu_2MnAl structure type. Appropriate substitutions may generate two beneficial features: (i) an intended modification and tuning of the eDOS and (ii) disorder in the crystal lattice, expected to distinctly decrease the lattice thermal conductivity of the material.

A variety of studies regarding substitutions, doping, or off-stoichiometric sample preparation has already been carried out previously and reported in the literature [5–13]. Most successful studies with respect to the thermoelectric performance, expressed by the dimensionless figure of merit $ZT = S^2/(\rho\lambda)$, where T is the absolute temperature, S is the Seebeck coefficient, ρ is the electrical resistivity, and λ is the thermal conductivity, have been undertaken by substituting Al by Si or Ge, V/W, and V/Mo. ZT values of up to about 0.2 have been obtained. Severe plastic deformation in $Fe_2VAl_{0.95}Ta_{0.05}$ caused a further increase of ZT to $ZT = 0.3$ [14].

The aim of the present work is to demonstrate such an advantageous tunability of Fe_2VAl by substituting V by W and, in addition, by making this substitution off-stoichiometric, i.e., changing $[Fe_{2/3}(V, W)_{1/3}]_{75}Al_{25}$ toward $[Fe_{2/3}(V, W)_{1/3}]_{76}Al_{24}$. In this study, experimentally derived results, obtained on samples up to 20% exchange of V by W, are presented and analyzed. These findings are compared and confronted with first-principles DFT calculations, allowing us to draw some microscopic picture of this series of alloys. Additionally, high temperature and high magnetic field Hall measurements, which have been carried out for this study,

allow us to conclude about the predominant charge carriers and their respective mobilities, as well as to derive their temperature dependencies at high temperatures. Such a study is lacking in the literature up to now.

This series of alloys constitutes the basis for magnetron sputtered thin film systems, which have recently been found to exhibit ZT values beyond those reported so far in literature [15]. A deeper understanding of relevant mechanisms and interactions of the electronic and thermal transport is thus of significance.

II. EXPERIMENTAL

$Fe_2V_{1-x}W_xAl$ alloys and off-stoichiometric variants (about 3.5 gram each) were prepared by high frequency melting of high purity starting materials on a water-cooled copper hearth under argon atmosphere. To ensure homogeneity of the samples, the melting process was repeated several times. Subsequently, all alloys were sealed in quartz tubes and annealed at 900 °C for one week.

X-ray powder diffraction data at room temperature from as-cast and annealed alloys were taken on a Siemens D5000 diffractometer employing Cu$K_{\alpha 1}$ radiation ($10^\circ < 2\Theta < 100^\circ$). Refinement of the crystal structures was performed with the program PowderCell.

The microstructure and composition of Fe_2VAl based full Heusler alloys were examined by scanning electron microscopy (SEM) using a Philips XL30 ESEM with an EDAX XL-30 EDX detector.

Measurements of the various physical properties were carried out with a series of standard techniques [16]. A commercially available setup (ULVAC, ZEM3) was used to study the electrical resistivity and the Seebeck coefficient above room temperature. The Hall resistance was derived above room temperature using the van der Pauw technique and employing a LakeShore 370 ac resistance bridge. Fields up to 10 T were generated by a superconducting magnet (Cryogenic, London) cooled by a closed cycle refrigerator.

III. COMPUTATIONAL ASPECTS

For the calculation of the density functional theory (DFT) results the Vienna *ab initio* simulation package (VASP) [17,18] with the projector augmented wave potential (PAW) [19,20] construction was applied. For approximating the exchange-correlation functional we made use of the generalized gradient approximation (GGA) of Ref. [21]. An energy cutoff for the plane wave basis of 600 eV was taken, while the finally chosen k-point mesh was $24\times24\times24$ points in the total Brillouin zone.

The potentials were constructed in such a way that for V and Fe the semicore states $3s^2$ and $3p^6$ were treated as valence states, resulting in 13 and 16 valence electrons, respectively. For W, with the $5d^4$ state and the semicore states $6s^2$ and $5p^6$, a total count of 12 valence electrons results. For Al the three valence states $3s^2$ and $3p^1$ were considered.

No spin-orbit coupling (SOC) was included because its influence on total energies and forces is usually negligible. On the other hand very accurate forces—as needed for the phonon calculations—converge substantially faster without SOC.

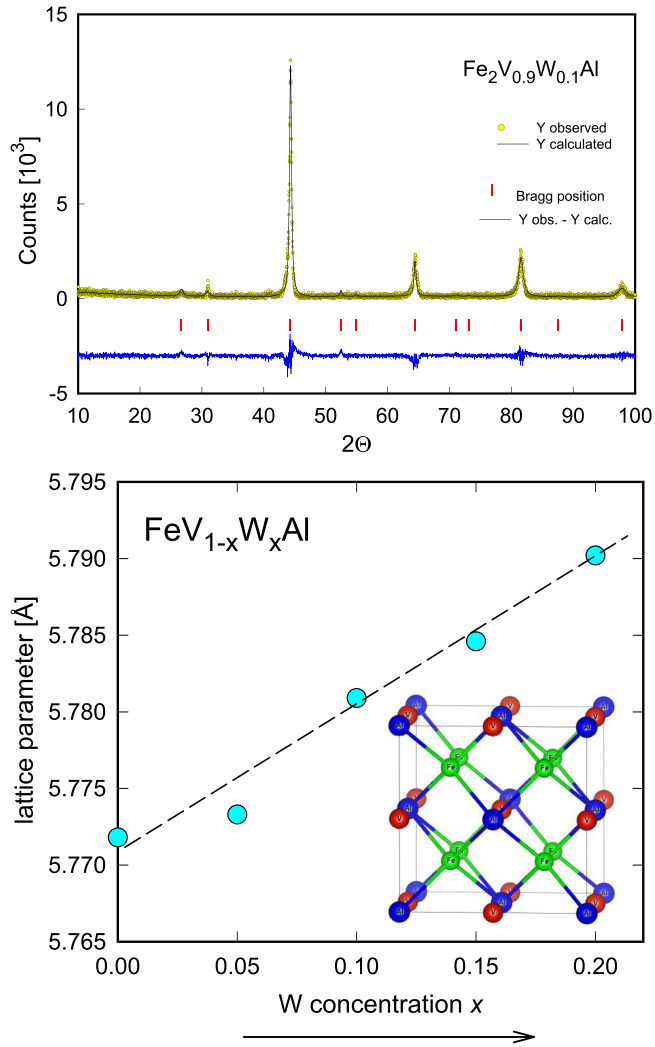

FIG. 1. Upper panel: X-ray diffraction pattern for $FeV_{0.9}W_{0.1}Al$ (filled circles), together with results from a Rietveld refinement (solid line), the difference between experimental and model data (lower part of the figure), and respective Bragg positions. Lower panel: Concentration dependence of the lattice parameter a of $FeV_{1-x}W_xAl$ taken at room temperature. The inset is a sketch of the crystal structure of Fe_2VAl.

Furthermore, typical electronic W states are found significantly lower or higher than Fermi energy (compare the eDOS of $Fe_2V_{1-x}W_xAl$, shown in Fig. 2) and therefore the influence of the heavy element W on SOC and thus on the transport properties is negligible.

Equilibrium volumes and atomic positions were derived from minimizing the total energies as a function of volume as well as atomic forces. The equilibrium lattice parameter of Fe_2VAl is $a = 5.689$ Å (volume per atom: $V_A = 11.514$ Å^3), of $Fe_2W_{0.125}V_{0.875}Al$, $a = 5.714$ Å^3 ($V_A = 11.66147$ Å^3), and of $Fe_2W_{0.25}V_{0.75}Al$, $a = 5.735$ Å^3 ($V_A = 11.78971$ Å^3). The DFT lattice parameter of Fe_2VAl agrees well (by 1.45%) with the experimental one of the present work, as well as with other DFT calculations [13,22].

For vibrational properties within the harmonic approximation the direct force constant method as implemented in

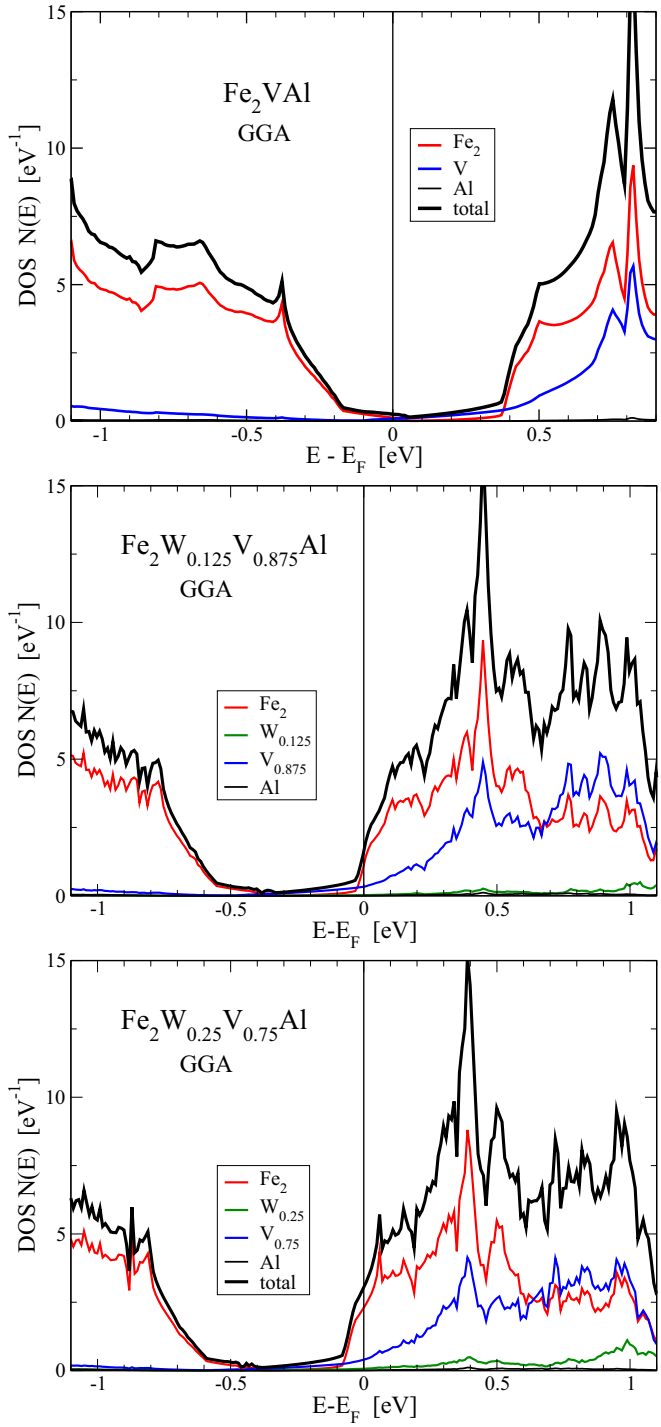

FIG. 2. Atom-like and total electronic density of states $N(E)$ near Fermi energy E_F. Upper panel: Fe_2VAl; central panel: $Fe_2V_{0.875}W_{0.125}Al$; lower panel: $Fe_2V_{0.75}W_{0.25}Al$. Results for W-doped compounds are derived from 32-atom supercell calculations at equilibrium volumes. Al-like DOS is zero around E_F and very small otherwise.

the program package *f*PHON was used [23,24]. For deriving the force constants density functional perturbation theory calculations as implemented in VASP were performed. Atomic positions were optimized until the residual forces were less than 2×10^{-5} eV/Å.

IV. RESULTS AND DISCUSSION

Figure 1, upper panel, shows an example of the x-ray diffraction pattern taken for the sample $x = 0.1$. The respective Rietveld refinement is shown in addition (solid line), together with the respective Bragg positions (vertical lines) and the difference between the experimental and the fitted data. Since besides the positions of the expected Bragg peaks no intensity is found in the respective x-ray data, good phase purity is evident.

In order to appropriately account for the intensities of the various Bragg peaks, the standard full Heusler structure (Cu_2MnAl type, space group No. 225) was slightly modified such that about 5% of Al is located at the V (4b) site and vice versa, 5% of V is located at the Al (4a) site. It is well known from the literature that different types of antisite occupations occur in Heusler systems; as a consequence, a variety of cubic structure types can be realized. Specifics of this interesting phenomenon are discussed in detail in Ref. [1]. Based on these Rietveld fits, the lattice parameters of the entire series were obtained; values are summarized in Fig. 1, lower panel, together with a sketch of the crystal structure of Fe_2VAl. Obviously, there is a monotonic increase of the lattice parameter a with increasing W content, as a result of the larger atomic radius of W (193 pm) with respect to V (183 pm).

Scanning electron microscopy (SEM) results regarding the elemental distribution of all samples in this study are very close to stoichiometry (about 1 at.%), when integrating over an area of 100×100 μm^2. SEM images, however, presumably reveal the presence of dendritic-like structures, and phases of two kinds: one is slightly richer in tungsten, while the other is less rich in W, compared to the intended composition [25].

Results of the first-principles electronic structure calculations carried out for $Fe_2V_{1-x}W_xAl$ are summarized in Fig. 2.

For stoichiometric Fe_2VAl, a pseudogap in the electronic density of states $N(E)$ is found. As particularly mentioned in the DFT study of Weinert and Watson [4] the Al-like DOS is zero in the nearer vicinity of E_F, and very small at larger/smaller energies as shown in all the DOSs in Fig. 2. This feature is important for the understanding of the bonding and electronic properties of states in the vicinity of E_F. These latter states primarily govern the electronic transport properties. The Fermi energy E_F is located right at the edge of the valence band. An estimation of the pseudogap width reveals values well below 1 eV. Below and above the pseudogap, there is a strong energy dependence of occupied and unoccupied states (see our previous study on $(Fe, Ni)_2VAl$ [26]).

The nonisoelectronic substitution of V by W provides extra electrons to the system; as a consequence, the Fermi level should rise. Indeed, this can be observed from the present DFT calculations carried out for the substituted samples in terms of supercells; i.e., the chemical composition $Fe_2V_{0.875}W_{0.125}Al$ would correspond to $Fe_{16}V_7WAl_8$ and $Fe_2V_{0.75}W_{0.25}Al$ is equivalent to $Fe_{16}V_6W_2Al_8$. Both samples are near real compositions of the present study. In both cases, E_F moves toward the edge of the conduction band, while the pseudogap structure is maintained. The color codes indicate that predominantly Fe contributes to the electronic densities in the vicinity of the pseudogap (more than 3 quarters); V states are below one quarter and W states are almost negligible (a

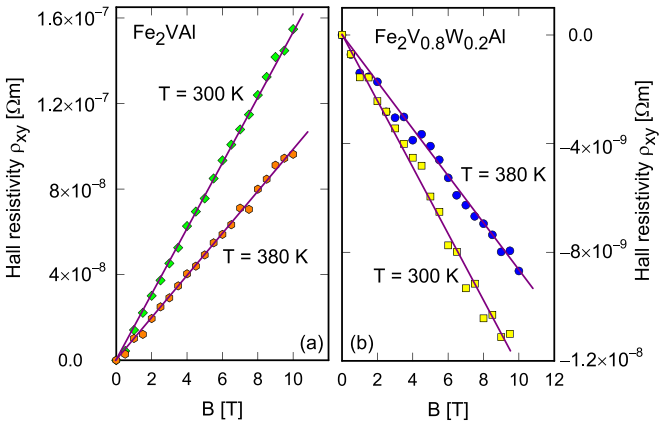

FIG. 3. Field dependent Hall resistivity ρ_{xy} of $Fe_2V_{1-x}W_xAl$ for $x = 0$ (left panel) and $x = 0.2$ (right panel) for various temperatures.

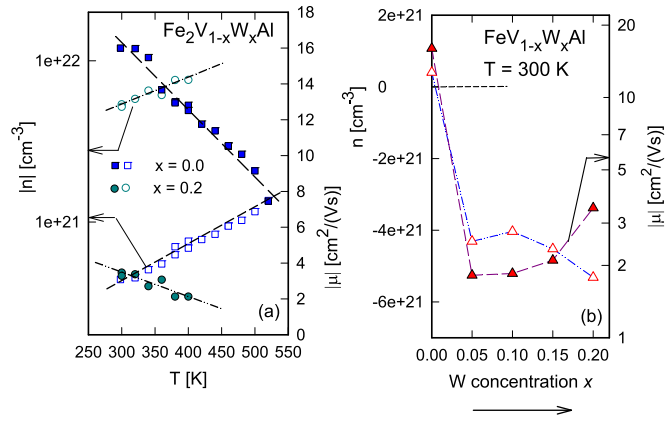

FIG. 4. (a) Temperature dependent absolute charge carrier density n (left axis) and absolute mobility μ (right axis) of $Fe_2V_{1-x}W_xAl$ for $x = 0$ and $x = 0.2$. (b) Charge carrier density n (left axis) and absolute mobility μ of $Fe_2V_{1-x}W_xAl$ for various concentrations of x, derived at room temperature.

faint maximum is present around 1 eV above E_F). The overall eDOS structure keeps pretty much the same, but the densities at the Fermi level almost double from $x = 0.125$ to $x = 0.25$, i.e., $N(E_F) \approx 1.5$ states/eV ($x = 0.125$), and $N(E_F) \approx 3$ states/eV ($x = 0.25$). Moreover, the slopes of $N(E_F)$ slightly flatten with increasing x. This might distinctly influence the absolute thermopower values. The shift of the Fermi energy from the valence band edge in the case of Fe_2VAl to the conduction band edge for finite W content should go along with a change of the majority charge carriers, from p-type to n-type electronic transport. This, in fact, is obvious from the present experimental data (see below).

A. Hall data

In order to qualitatively and quantitatively check the results of electronic structure calculations and to obtain information about the mobility of the charge carriers, Hall measurements were carried out and analyzed in terms of the classical single band model.

Shown in Fig. 3 are Hall measurements carried out at $T = 300$ and 380 K as typical examples of our measurements and fields up to 10 T. Obviously, the Hall resistance ρ_{xy} is different for Fe_2VAl and the W substituted system. While the former is positive and increases linearly with field, the latter is negative for the entire field range up to 10 T. These observations allow us to conclude the following: (i) There is for both materials a predominating charge carrier type. Thus, all analyses can be done in terms of the classical single band model. (ii) The positive Hall resistivity ρ_{xy} of Fe_2VAl refers to holes as the dominating carriers, while the negative one of $Fe_2V_{0.8}W_{0.2}Al$ is indicative of electrons. The charge carrier concentration n in the single band model follows from $\rho_{xy} = B/(\pm qn)$, where B is the magnetic field and q is the unit charge of the charge carriers. The mobility μ is then simply given by $\mu = \rho_{xy}/(\rho_{xx}B)$; ρ_{xx} represents the ordinary (longitudinal) electrical resistivity. Both the charge carrier densities and the mobilities are summarized in Fig. 4, left panel, for temperatures up to 520 K. Obviously, for both samples, the charge carrier concentration grows substantially with increasing temperature, as a result of excitations of carriers across the narrow gap in the density of states. Rising $n(T)$ in conjunction with the observed electrical resistivity causes a decrease of the mobility μ, Fig. 4(a), right axis.

Comparing $x = 0$ with the substituted sample $x = 0.2$ reveals that the W substituted sample exhibits a charge carrier density n, which is almost one order of magnitude larger than that of Fe_2VAl, while the opposite occurs for the mobility μ, which is significantly lower for the substituted alloy.

The rather small carrier concentration for $x = 0$ ($n_h \approx 4\times10^{20}$ cm^{-3}) at $T = 300$ K convincingly corroborates our DFT results and the positive signature refers to the Fermi energy located in the tail of the valence band with very small but finite values of the eDOS. In addition, this positive numerical value is in excellent agreement with earlier reports deduced from limited field ranges ($B < 1.5$ T) [5,27]. Because of the fully ordered structure in ternary Fe_2VAl, the mobility of the holes is high since the number of scattering events is reduced. On the other hand, even small substitutions of V/W drive the Fermi energy across the pseudogap into the tail of the conduction band. Electrons are then the main carriers (compare Fig. 4, right panel, $T = 300$ K), as also evidenced from the DFT results of Fig. 2. In fact, all W substituted alloys exhibit negative charge carriers and thus a negative value of the mobility. The charge carrier density of the W substituted alloys slightly increases with increasing x, while the mobility in each case is much smaller than in the starting material.

The almost linear dependence of the field dependent Hall resistivity ρ_{xy} refers to a dominating type of charge carrier, i.e., to electrons, where the d electrons of Fe, V, and W are supposed to be the relevant ones, governing the mobility.

A comparison of the respective electronic densities of states obtained for V/W substituted and nonsubstituted samples in the present series shows that in *each* case Fe and V d states dominate the density right at the Fermi energy. Tungsten d states are, however, negligible in the proximity of the respective Fermi energies (see Fig. 2). Thus, one expects that the mobilities related to the d electrons do not change substantially upon the V/W substitution.

Presumably, the observed increase of mobility of the substituted samples (i.e., from $x = 0.05$ to $x = 0.2$) is then likely

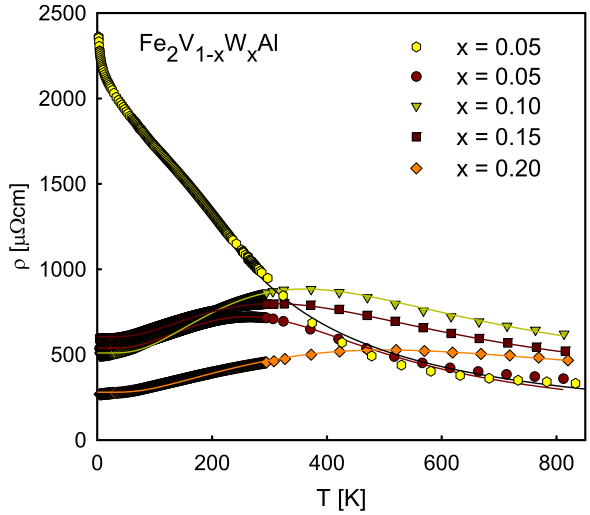

FIG. 5. Temperature dependent electrical resistivity ρ of $Fe_2V_{1-x}W_xAl$ for various concentrations x. The solid lines are least squares fits (see the text).

due to a change in the balance of the mobilities related to impurity and phonon scattering. Following Matthiessen's rule, the overall mobility μ can be expressed as

$$\mu = \frac{1}{\frac{1}{\mu_{\text{impurity}}} + \frac{1}{\mu_{\text{phonon}}}}. \quad (1)$$

Because of the increasing degree of static disorder due to the V/W substitution, μ_{impurity} is expected to decrease when proceeding from $x = 0.05$ to $x = 0.2$. However, in order to trace the observed increase of μ, the mobility related to the electron-phonon interaction needs to grow, overcompensating the former [compare Eq. (1)]. In fact, the lattice of $Fe_2V_{1-x}W_xAl$ softens upon increase of x as is obvious from the evolution of the Debye temperature (compare Sec. IV D) and thus the electron-phonon interaction might weaken as well, leading to enhanced mobilities. The fairly intricate interplay of several components, however, makes a definite explanation of the Hall data all but impossible.

B. Electrical resistivity

Shown in Fig. 5 is the temperature dependent electrical resistivity ρ for various concentrations of W in $Fe_2V_{1-x}W_xAl$. Obviously, $\rho(T)$ of this series neither follows a simple metallic behavior nor is characterized by a typical semiconducting one. Rather, a subtle overlay of both scenarios is quite likely; hence the temperature dependent resistivity of the present samples consists of metallic-like and semiconducting-like contributions, together with faint, sample dependent maxima in $\rho(T)$. The more semiconducting-like temperature dependence of $\rho(T)$ above room temperature coincides with measurements of Mikami *et al.* [9]. There, however, no low temperature data were reported.

The distinct behavior of $\rho(T)$ as presented in Fig. 5 can be accounted for in terms of a temperature dependent charge carrier density in the context of electron-phonon and electron-static imperfection interactions. A model with a simplified electronic density of states, which we have developed previously (for details see, e.g., Ref. [26]), was successfully applied to various skutterudites, clathrates, and half Heusler systems, and recently also to the Heusler series $Fe_{2-x}Ni_xVAl$ [26]. Least squares fits of the model described above to the experimental data have been carried out; results are shown as solid lines in Fig. 5. Over a very broad range of temperatures, the fits reveal convincing agreements and many material related parameters, characterizing these thermoelectric materials.

Comparing $\rho(T)$ of various concentrations, several trends are obvious. The almost semiconducting-like resistivity of starting Fe_2VAl crosses over to a feature with a smooth maximum in $\rho(T)$ at $T_\rho^{\max}$. The latter increases with increasing W concentration. Forming a maximum in $\rho(T)$ is due to the thermal excitation of electrons across the gap in the eDOS of the system. Qualitatively, this means that the gap of the series grows with growing W content. In fact, the least squares fits reveal an increase of the gap, from about 45 meV for Fe_2VAl to 205 meV for the sample with $x = 0.2$. The resulting $\rho(T)$ curve itself is a subtle balance of the growing charge carrier density, as the temperature increases, with respect to the increasing resistivity contribution owing to the electron-phonon interaction upon an increasing temperature. Moreover, the increasing charge carrier concentration with increasing W content competes with the tendency of the lattice to become more disordered, which would enlarge the residual resistivity owing to the V/W substitution.

Following the evolution of the electronic density of states, the substantially reduced eDOS of Fe_2VAl at E_F slightly below the pseudogap causes an almost simple semiconducting behavior; the temperature dependence, however, does not coincide with a simple exponential decay. The increase of the W content causes a change from hole to electron type charge carriers, together with a density increase. This causes, overall, a decrease of the absolute resistivity values and a slight shift of the maxima toward higher temperatures. Obviously, since the sample with the largest W concentration exhibits the lowest electrical resistivity in the entire temperature range, the increase in disorder scattering is supposed to be overcompensated by an increase of the charge carrier concentration due to the V/W substitution. The latter is in agreement with results from Hall measurements (compare Fig. 4).

C. Thermopower

The temperature dependent thermopower S is summarized in Fig. 6 for temperatures in a range from 4 K to about 800 K. It is interesting to note that the absolute thermopower values, e.g., around 300 K, trace the behavior of the charge carrier density as observed from the Hall data (Fig. 3), where the smallest n values (around $x = 0.1$) reveal the largest thermopower, about $-150\ \mu$V/K. Seebeck values of about the same size and concentration dependence for temperatures above room temperature were reported previously by Mikami *et al.* [9], corroborating the present data, as well as a comparable sample quality of the substituted alloys. As already indicated from both the Hall effect as well as from the electronic structure calculations, the V/W substitution is responsible for a change of the charge carrier type, from hole dominated (Fe_2VAl) to electron dominated transport. As a consequence, thermopower changes sign, from positive

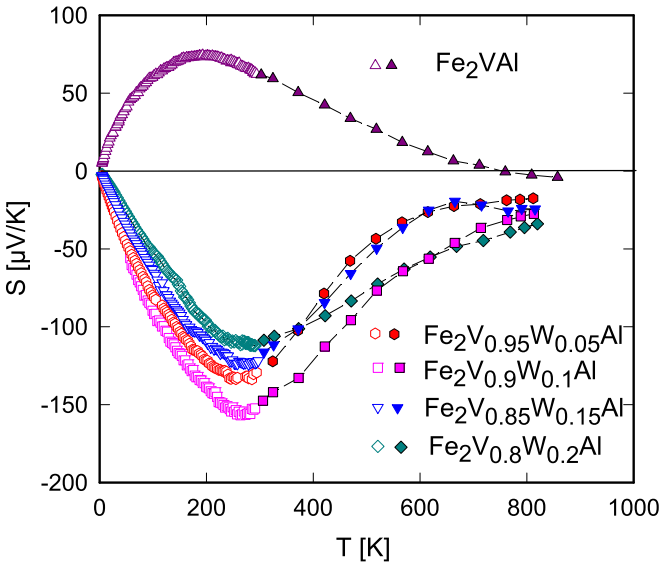

FIG. 6. Temperature dependent thermopower S for various concentrations x of $Fe_2V_{1-x}W_xAl$.

(Fe_2VAl) to negative (W substituted samples). This becomes obvious, too, from Mott's theory of thermopower,

$$S(T) = \mathcal{C}T \frac{1}{N(E)} \frac{\partial N(E)}{\partial E}\bigg|_{E=E_F}, \tag{2}$$

which indicates that the sign and the absolute thermopower values are determined by the logarithmic derivative of the density of states with respect to energy at the Fermi energy. In Eq. (2), $\mathcal{C}$ is a constant. Taking into account Eq. (2) in the context of the eDOS of the present materials (compare Fig. 2) would provoke larger $S(T)$ values for $x = 0.1$ than for $x = 0.2$, since $N(E_F)$ is larger in the latter and $\partial N(E)/\partial E)|_{E=E_F}$ is smaller.

The simple overall behavior of $S(T)$ as inferred from Eq. (2), however, becomes modified from the fact that the observed thermopower not only consists of contributions from a single charge carrier type. Rather, because of the relatively narrow gap in $N(E)$ next to the Fermi energy, both electrons and holes are becoming actively involved, i.e.,

$$S = \frac{\sigma_h S_h + \sigma_e S_e}{\sigma_h + \sigma_e}. \tag{3}$$

Here, $\sigma_{h,e}$ and $S_{h,e}$ are the electrical conductivities and the Seebeck coefficients of holes and electrons, respectively. Equation (3) indicates that the measured thermopower data of narrow gap semiconductors might exhibit quite complicated temperature dependencies, where the almost linear temperature dependence as inferred from Eq. (2) can become dramatically modified from the temperature dependent change of the charge carrier density n as well as from the electron-phonon interaction, resulting in a lowering of the electrical conductivity of a certain system as the temperature increases. Various measurements carried out on doped/substituted Fe_2VAl samples demonstrate a behavior which is similar to the one of Fig. 6, including changes from positive to negative values (compare, e.g., Refs. [10,28,29]).

The Seebeck coefficient of narrow gap semiconductors exhibits very frequently extrema in its temperature dependence. According to Ref. [30], the gap in the eDOS, E_g, near E_F is related to the maximum value of the thermopower at that temperature $T^S_{\max}$ according to

$$E_g = 2e|S_{\max}|T^S_{\max}. \tag{4}$$

Here, e is the electron charge and $S_{\max}$ the thermopower at the maximum in the $S(T)$ curve at a temperature $T^S_{\max}$. This extremum is a consequence of a bipolar conduction mechanism, involving thermal excitations of holes and electrons across the band gap. The sign change of $S(T)$ of starting material Fe_2VAl at elevated temperatures is thus a result of the promotion of electrons across the gap in the eDOS near the Fermi energy E_F.

Applying Eq. (4) to the experimental data of Fig. 6 allows us to derive a rough estimation of the pseudogap, revealing 14.3, 32.3, 40, 32, and 31 meV for $x = 0.0$, 0.05, 0.1, 0.15, and 0.2, respectively. However, care has to be taken regarding the value of the gap width estimated from Eq. (4). As pointed out by Gibbs *et al.* [31] significant failures can occur in those cases, where $|S_{\max}| \leqslant 150\ \mu$V/K. In fact, all samples studied here exhibit thermopower values around or below this critical number.

D. Phonon dispersion and thermal conductivity

Measurements of the temperature dependent thermal conductivity λ of Fe_2VAl based alloys reported so far (see, e.g., Refs. [5,6]) demonstrate that the lattice thermal conductivity dominates the overall measured quantity. Hence, the knowledge of the vibrational properties in such materials is of importance to understand the respective behavior. We have carried out DFT calculations in order to obtain reliable dispersion and phonon density of states data of these materials. Vibrational properties of $Fe_2V_{1-x}W_xAl$ were derived in the harmonic approximation employing the direct force constant method as implemented in the program package *f* PHON [23,24]. For deriving the force constants, density functional perturbation theory calculations as implemented in VASP were performed. Atomic positions were optimized until the residual forces were less than 2×10^{-5} eV/Å. For anharmonic contributions, a quasiharmonic approach was applied [32,33]. For this approach, bulk moduli are needed which amount to 207 GPa for Fe_2VAl, 218 GPa for $Fe_2V_{0.875}W_{0.125}Al$, and 226 GPa for $Fe_2V_{0.75}W_{0.25}Al$.

In order to obtain reliable phonon data for the W substituted systems, $2\times2\times2$ supercells have been constructed such that $Fe_{16}W_1V_7Al_8$ corresponds to $Fe_2V_{0.875}W_{0.125}Al$ and $Fe_{16}W_2V_6Al_8$ corresponds to $Fe_2V_{0.75}W_{0.25}Al$. Results are presented for the respective DFT volumes in Fig. 7.

The acoustic branches in Fe_2VAl (Fig. 7, upper panel) form the quite shallow part up to 6 THz, followed by optical branches. Above a gap of about 2 THz, almost dispersionless Al branches are located. Relevant parameters with respect to thermal conductivity are the sound velocities [2 transversal ($v_{t1,t2}$) and one longitudinal contribution (v_l)] as well as the Debye temperatures. These data are collected in Table I for Fe_2VAl.

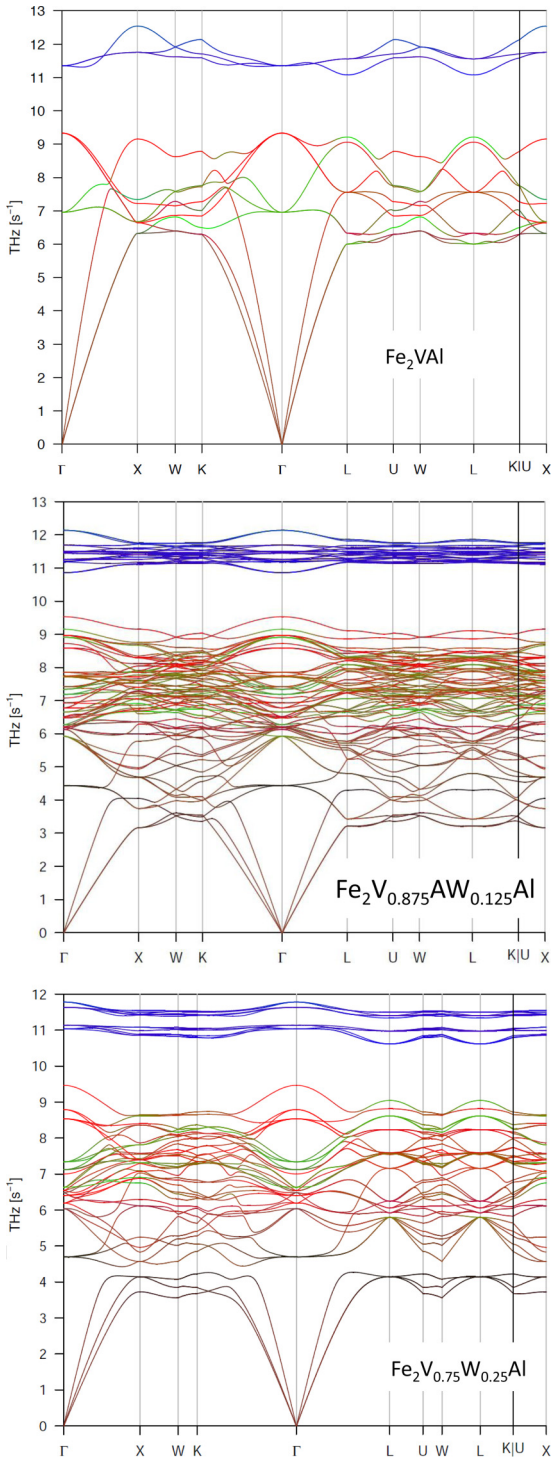

FIG. 7. Calculated $\vec{q}$ dependent phonon dispersion at DFT equilibrium volumes weighted according to local atomic contributions (Fe, red; V, green; Al, blue; W, black; mixed colors indicate mixed contributions). Upper panel: Fe_2VAl; middle panel: $Fe_2V_{0.875}W_{0.125}Al$; lower panel: $Fe_2V_{0.75}W_{0.25}Al$.

Substituting V/W reveals various changes of the overall phonon dispersion [Figs. 7 middle panel and 7 lower panel]: (i) The acoustic phonon branches are less steep in comparison to the starting material. As a consequence, the average sound velocity reduces from 5263 to 4908 and finally to 4632 m/s

TABLE I. Calculated velocities of sound v_s at 300 K for DFT equilibrium. Values given for the three acoustic modes (l: longitudinal; $t1, t2$: transversal) and the mode average $\bar{v}_s$, the Debye temperature θ_D, and the bulk modulus B_0.

	Fe_2VAl	$Fe_2V_{0.875}W_{0.125}Al$	$Fe_2V_{0.75}W_{0.25}Al$
v_{t1} (m/s)	4568	4247	4013
v_{t2} (m/s)	4970	4642	4377
v_l (m/s)	8018	7551	7234
$\bar{v}_s$ (m/s)	5263	4908	4720
B_0 (GPa)	207	218	226
θ_D (K)	696	644	606

for $x = 0,\ 0.125,\ 0.25$, respectively (compare Table I). As the thermal conductivity is a function of the sound velocity, a decrease of $\lambda(T)$ in this sequence can be expected without considering any further scattering processes. Interestingly, the acoustic branches get very flat in the range of about 4 THz, driven mostly from W vibrations. (ii) The optical branches are lowered upon the increasing W content, too. A gap opens in the case $x = 0.25$ between the acoustic and optical branches and the Al bands lower slightly in both substituted systems. Due to the usage of supercells, containing many more atoms, the number of optical branches increases as a consequence. The lower lying optical bands result from Einstein-like vibrations, which might constitute additional scattering of the heat carrying phonons; hence, the thermal conductivity of the W substituted alloys is expected to further decrease. (iii) the Grüneisen parameter Γ is increasing as well for an increasing W content. Since the lattice thermal conductivity λ_{ph} depends on Γ, i.e., $\lambda_{ph} \propto 1/\Gamma^2$, an additional decrease of thermal conductivity is expected. Note that Γ accounts for the anharmonicity of lattice effects.

These three scenarios obtained from our DFT calculations infer that modifications of the phonons intrinsically lead to a reduction of the lattice thermal conductivity. Besides, enhanced scattering of the heat carrying phonons on increased static disorder in the lattice due to the random distribution of V and W on the (4a) sites of the Cu_2MnAl type structure is expected. Primarily mass and size differences between V and W matter.

The average velocities of sound $\bar{v}_s$ and the Debye temperatures were obtained according to Ref. [34]. As discussed previously [26], the DFT related values of Fe_2VAl are larger than those directly derived from measurements of the sound velocity, but roughly agree with heat capacity studies. The concentration dependent variation of data, however, is very reasonable. Due to the V/W substitution, the strength of the material increases, as expressed by the bulk modulus B_0, while the increase of mass upon the increase of the W content reduces the sound velocities and thus the Debye temperatures, too, by about 10% for the 20% exchange of V/W.

The temperature dependent thermal conductivity λ of $Fe_2V_{1-x}W_xAl$ is plotted in Fig. 8 for various concentrations x. It is well known from the literature that $\lambda(T)$ of Fe_2VAl is, at least in certain temperature ranges, roughly 40 to 50 times larger than that of archetypal Bi_2Te_3. It is, in the most simplest picture, a consequence of the very large sound

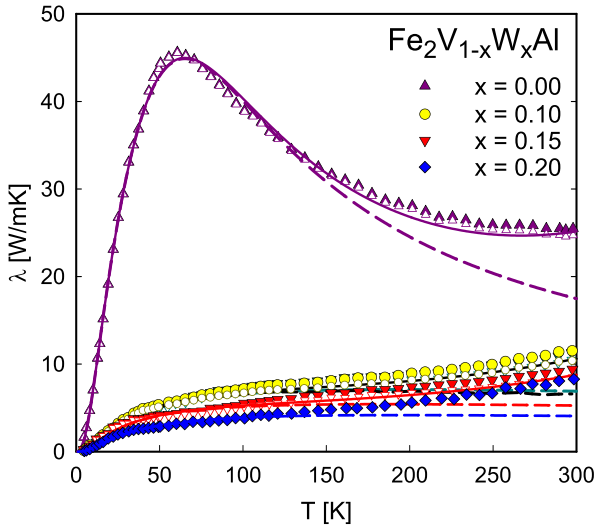

FIG. 8. Temperature dependent thermal conductivity λ for various concentrations x of $Fe_2V_{1-x}W_xAl$. The solid and dashed lines are least squares fits as explained in the text.

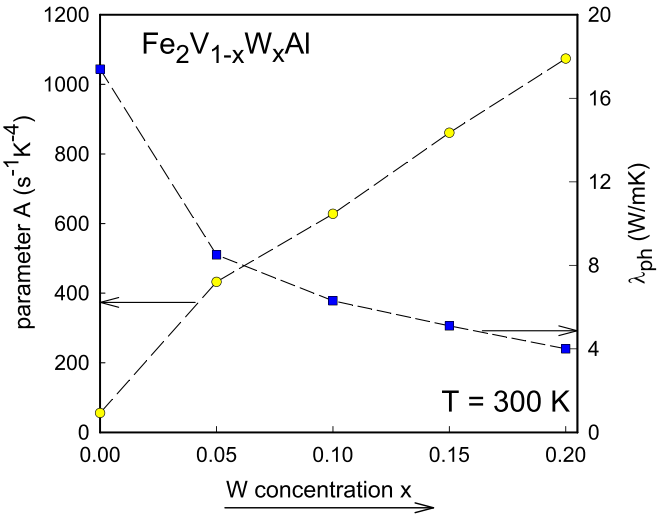

FIG. 9. Concentration dependent point defect scattering parameter A of $Fe_2V_{1-x}W_xAl$ [compare Eq. (7)] (left axis) and lattice thermal conductivity λ_{ph} taken at room temperature.

velocity (more than 5200 m/s) and the relative simple type of crystal structure. As already discussed in the previous paragraph, the V/W substitution causes an intrinsic decrease of $\lambda_{ph}(T)$, together with improved scattering on point defects from the disorder at the (4a) sites. In fact, these mechanisms substantially influence $\lambda(T)$ as can be seen from the large overall drop of $\lambda(T)$ in the experimental data.

In a standard procedure, as described in many details, e.g., in our recent work on $Fe_{2-x}Ni_xVAl$ [26], the thermal conductivity can be analyzed and proper conclusions can be drawn. The lattice thermal conductivity follows simply from $\lambda_{ph} = \lambda - \lambda_e$, where the subscript e refers to the electronic thermal conductivity.

In order to obtain the electronic thermal conductivity λ_e, the Wiedemann-Franz law can be employed, relating the electrical resistivity ρ to λ_e by $\lambda_e \rho = L_0 T$. Here,

$$L_0 = \frac{\pi^2}{3}\left(\frac{k_B}{e}\right)^2 = 2.45\times10^{-8}\ \mathrm{W\,\Omega\,K^{-2}} \qquad (5)$$

is the Lorenz number. Taking into account the experimental data of Fig. 5, the respective λ_e values can be estimated (compare Fig. 8). Obviously, λ_e is small in all cases; its contribution is just a few percent to the overall measured effect. The analysis of the remaining part, $\lambda - \lambda_e$, is carried out in the context of Callaway's theory [35], where phonons are treated in terms of the Debye model, and scattering processes are accounted for by a total relaxation time, $1/\tau_c = \sum 1/\tau_i$. The individual scattering processes are considered independently from each another and are characterized by distinct temperature and frequency dependencies [35].

The Callaway model can be expressed as [36]

$$\lambda_{ph} = \frac{k_B}{2\pi^2 v_s}\left(\frac{k_B T}{\hbar}\right)^3 \int_0^{\theta_D/T} \frac{x^4 \exp(x)}{\tau_c^{-1}[\exp(x)-1]^2} dx. \qquad (6)$$

$x = \hbar\omega/(k_B T)$, k_B is the Boltzmann constant, and ω is the phonon frequency; $\hbar = h/(2\pi)$. τ_c for the relevant phonon scattering processes is given by

$$1/\tau_c = v_s/L + A\omega^4 + B\omega^2 T \exp(-\theta_D/T) + E\omega, \qquad (7)$$

where the terms on the right-hand side of Eq. (7) refer to scattering on grain boundaries with average size L, on point defects, umklapp processes, and electrons, respectively. A, B, and E are material dependent constants. Least squares fits according to Eqs. (6) and (7) have been performed and the results are shown in Fig. 8 as solid and dashed lines. Adding a T^3 term to account for radiation losses [37], inherent to the steady state heat flow technique, reveals a fairly good agreement between experiment and theory. In all cases, the sound velocity and the Debye temperature were changed linearly from $x = 0 \rightarrow x = 0.20$ as inferred from the DFT results.

The parameters derived from these least squares fits allow us to trace, among others things, the evolution of the point defect scattering parameter A as a function of the W concentration (compare Fig. 9, left axis). This demonstrates that W constitutes a significant scattering center, as this parameter grows substantially by more than one order of magnitude. This is about twice as large as observed in a similar study concerning the Fe/Ni substitution in $(Fe, Ni)_2VAl$ [26] and can be attributed to much larger mass/volume differences between V and W compared to Fe and Ni. Because of this significant enhancement of scattering on point defects, as well as intrinsic parameters like the sound velocity, the thermal conductivity drops to below a quarter of the value of Fe_2VAl at $T = 300$ K for the system with 20% V exchanged by W (compare Fig. 9, right axis). These values deduced at room temperature are in almost perfect agreement with the recent study of Mikami *et al.* [9], where λ_{ph} of the sample $x = 0.1$ reaches about 4 W/(m K).

The efficiency of point defect scattering is a result of contributions from mass fluctuations and volume differences of atoms on certain sublattices of the crystal structure. In general, it can be expressed by a disorder parameter Γ as

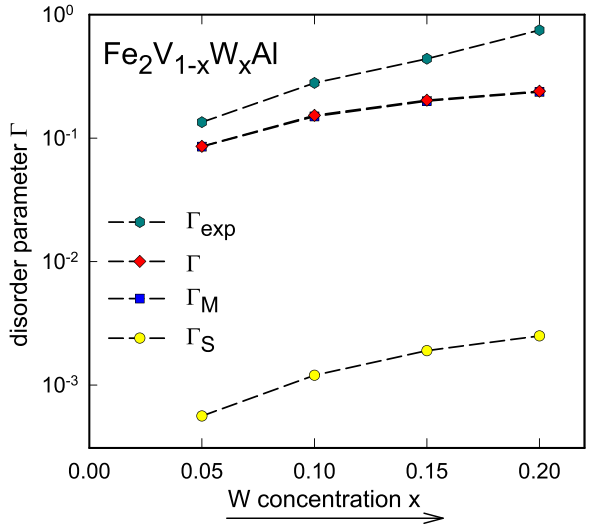

FIG. 10. Concentration dependent disorder parameter of $Fe_2V_{1-x}W_xAl$ derived experimentally (Γ_{exp}) and theoretically (Γ); the latter consists of a mass (Γ_M) and volume related contribution (Γ_S).

$\Gamma = \Gamma_M + \Gamma_S$, where the subscripts M and S refer to mass and strain field, respectively [38].

Following the procedure as outlined in Refs. [26,38] reveals a substantial contribution from mass differences between V and W, almost 2 orders of magnitude larger than the respective contribution due to size differences (Fig. 10). The parameter Γ_{exp} is derived from the experimental thermal conductivity data, as described in detail by Yang *et al.* [39]. The gap between Γ_{exp} and Γ is closed by an empirical factor (in general between 10 and 100) [38], accounting for an appropriate prefactor of the strain field contribution. Mikami *et al.* have analyzed their data in a similar manner and found that the strain-field contribution is twice as large as the mass contribution [9]. This, however, seems not to be meaningful, since the difference of the metallic radii between W and V is smaller than 3%, while W has a more than 3 times larger mass than V. It is thus very likely that the predominant contribution is due to the mass difference between V and W as derived in the present analysis (compare Fig. 9).

E. Thermoelectric performance

The relatively large Seebeck values and moderate electrical resistivities observed in $Fe_2V_{1-x}W_xAl$ samples cause that the power factors p_f of the four samples studied are ranging between 1.6 and 2.55 mW/(m K^2). These values are large and compare with those of nonoptimized Bi_2Te_3 systems. The figure of merit, ZT, remains modest because of the still large thermal conductivities but reaches $ZT \approx 0.20$ for $x = 0.1$. While Bi_2Te_3 based materials have thermal conductivities, ranging between 1 and 4 W/(m K), the room temperature value found for $Fe_2V_{0.8}W_{0.2}Al$ is of the order of 4 W/(m K). The reduction of λ(300 K) to about 25% of its initial value in Fe_2VAl is besides intrinsic changes of the phonon system a result of point defect scattering enhanced by the V/W exchange.

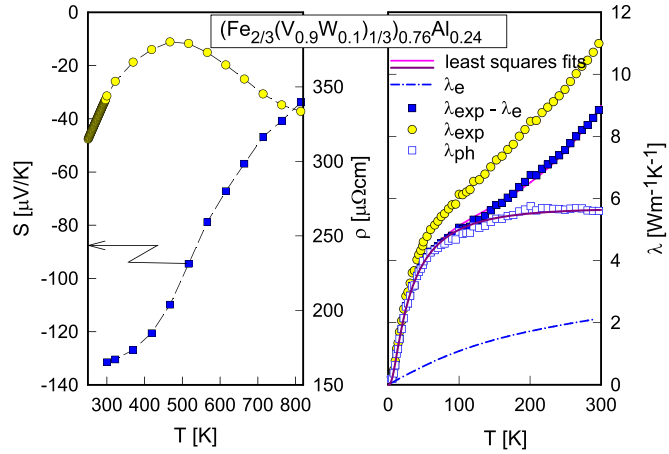

FIG. 11. Left panel: Temperature dependent Seebeck coefficient S (left axis) and temperature dependent electrical resistivity ρ of $[Fe_{2/3}(V_{0.9}W_{0.1})_{1/3}]_{0.76}Al_{0.24}$. Right panel: Temperature dependent thermal conductivity λ of $[Fe_{2/3}(V_{0.9}W_{0.1})_{1/3}]_{0.76}Al_{0.24}$. The electronic and lattice thermal conductivity are added together with least squares fits according to Eqs. (4) and (5).

F. Off-stoichiometric W based Heusler systems

Besides substitution and doping of a certain starting material, e.g., Fe_2VAl, off-stoichiometric preparation, i.e., $Fe_2V_{1\pm x}Al_{1\mp x}$, was already employed and distinct changes in the electronic and thermal transport were obtained. Here, we combine the substitution of V by W with off-stoichiometric preparation. As an example, $[Fe_{2/3}(V_{0.9}W_{0.1})_{1/3}]_{0.76}Al_{0.24}$ is chosen. Experimental results are shown in Figs. 11 and 12. Remarkably, the overall electrical resistivity ρ is small, only about half of the respective stoichiometric compound. Its temperature dependence is, again, a combination of metallic and semiconducting-like contributions. In addition, the charge carrier density $n_e = 4\times10^{21}$ cm^{-3} is almost equal. This refers to a substantially higher mobility of electrons in this sample. The Seebeck effect around room temperature, on the other

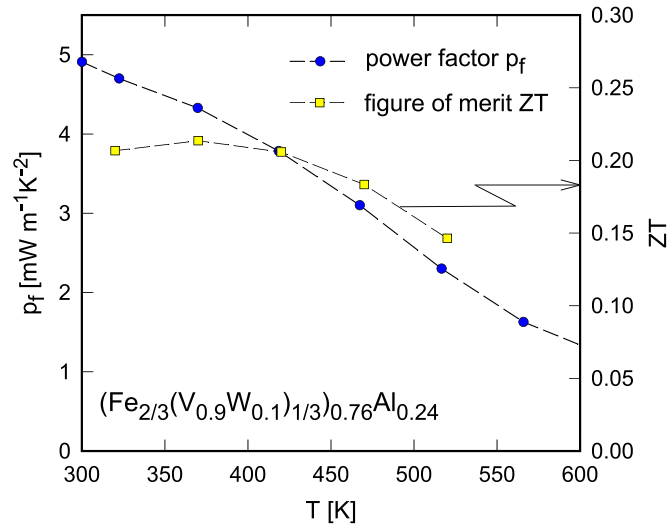

FIG. 12. Temperature dependent power factor p_f (left axis) and figure of merit ZT (right axis) of $[Fe_{2/3}(V_{0.9}W_{0.1})_{1/3}]_{0.76}Al_{0.24}$.

hand, is large, about $-135\ \mu$V/K, indicating electrons as primary charge carriers. The temperature dependent thermal conductivity is similar to the equivalent stoichiometric system and the phonon contribution λ_{ph} at room temperature coincides within about 10%. As a consequence, the power factor p_f (compare Fig. 12) appears to be extraordinarily large, exceeding best behaving Bi_2Te_3 at ambient pressure [40]. In the context of the reduced thermal conductivity observed, the figure of merit, $ZT = 0.22$, is one of the largest ever obtained ZT values of full Heusler systems. Here, it should be noted that while the under-stoichiometric systems (i.e., Al_{24}) are electron dominated, the over-stoichiometric systems, i.e., Al_{26}, are hole dominated. This indicates that small changes of the element contents in Fe_2VAl based Heusler systems might have dramatic effects on the electronic structure and thus on electronic and thermal transport.

V. SUMMARY

The substitution of V/W in the full Heusler series $Fe_2V_{1-x}W_xAl$ is responsible for a distinct change of electronic and thermal transport. This is caused by the movement of the Fermi energy from the valence band edge in Fe_2VAl across the band gap toward the conduction band, as proven from Hall and Seebeck effect measurements and confirmed by DFT calculations of the electronic structure (band dispersion and electronic density of states, eDOS). Since the Fermi energy is located at steep slopes of the eDOS, large Seebeck values are expected, and in fact are found experimentally.

Besides modifications of the electronic structure, the phonon system of the substituted samples changes as well. This results primarily in a reduction of the various values of sound velocities, a decrease of the Debye temperature, and an increase of the Grüneisen parameter. These changes drive an intrinsic decrease of the overall thermal conductivity. However, point defect scattering, mainly because of the lattice disorder created by the statistical distribution of V and W on the (4a) site of the Cu_2MnAl structure, reveals an additional contribution to the reduction of $\lambda(T)$ because of large mass and volume differences between V and W. As a result thermal conductivity for the sample $x = 0.2$ drops to about 25% of its initial value deduced for $x = 0$. This is a much stronger reduction (almost a factor of 2) compared to a similar substitution study of Fe/Ni in Fe_2VAl [26].

ACKNOWLEDGMENTS

Research was supported by the Christian Doppler Laboratory for Thermoelectricity and the Japan Science and Technology Agency (JST), programms CREST (JPMJCR19Q4) and MIRAI (JPMJMI19A1). DFT and related calculations were performed on the Vienna Scientific Cluster VSC3.

[1] T. Graf, C. Felser, and S. S. Parkin, Prog. Solid State Chem. **39**, 1 (2011).
[2] *Heusler Alloys: Properties, Growth, Applications*, edited by C. Felser and A. Hirohata, Springer Series in Materials Science Vol. 222 (Springer International Publishing, Cham, 2016).
[3] L. Wollmann, A. K. Nayak, S. S. P. Parkin, and C. Felser, Annu. Rev. Mater. Res. **47**, 247 (2017).
[4] M. Weinert and R. E. Watson, Phys. Rev. B **58**, 9732 (1998).
[5] Y. Nishino, S. Deguchi, and U. Mizutani, Phys. Rev. B **74**, 115115 (2006).
[6] C. S. Lue, C. F. Chen, J. Y. Lin, Y. T. Yu, and Y. K. Kuo, Phys. Rev. B **75**, 064204 (2007).
[7] M. Mikami and K. Kobayashi, J. Alloys Compd. **466**, 530 (2008).
[8] M. Mikami, S. Tanaka, and K. Kobayashi, J. Alloys Compd. **484**, 444 (2009).
[9] M. Mikami, Y. Kinemuchi, K. Ozaki, Y. Terazawa, and T. Takeuchi, J. Appl. Phys. **111**, 093710 (2012).
[10] K. Renard, A. Mori, Y. Yamada, S. Tanaka, H. Miyazaki, and Y. Nishino, J. Appl. Phys. **115**, 033707 (2014).
[11] M. Mikami, M. Inukai, H. Miyazaki, and Y. Nishino, J. Electron. Mater. **45**, 1284 (2016).
[12] P.-C. Wei, T.-S. Huang, S.-W. Lin, G.-Y. Guo, and Y.-Y. Chen, J. Appl. Phys. **118**, 165102 (2015).
[13] H. Al-Yamani and B. Hamad, J. Electron. Mater. **45**, 1101 (2016).
[14] S. Masuda, K. Tsuchiya, J. Qiang, H. Miyazaki, and Y. Nishino, J. Appl. Phys. **124**, 035106 (2018).
[15] B. Hinterleitner, I. Knapp, M. Poneder, Y. Shi, H. Müller, G. Eguchi, M. Eisenmenger, Ch. Stöger-Pollach, Y. Kakefuda, M. Kawamoto, Q. Guo *et al.*, Nature (London) **576**, 85 (2019).
[16] E. Bauer, S. Berger, C. Paul, M. D. Mea, G. Hilscher, H. Michor, M. Reissner, W. Steiner, A. Grytsiv, P. Rogl *et al.*, Phys. Rev. B **66**, 214421 (2002).
[17] G. Kresse and J. Furthmüller, Comput. Mater. Sci. **6**, 15 (1996).
[18] G. Kresse and J. Furthmüller, Phys. Rev. B **54**, 11169 (1996).
[19] P. E. Blöchl, Phys. Rev. B **50**, 17953 (1994).
[20] G. Kresse and D. Joubert, Phys. Rev. B **59**, 1758 (1999).
[21] J. P. Perdew and Y. Wang, Phys. Rev. B **45**, 13244 (1992).
[22] V. Kanchana, G. Vaitheeswaran, Y. Ma, Y. Xie, A. Svane, and O. Eriksson, Phys. Rev. B **80**, 125108 (2009).
[23] D. Alfè, Comput. Phys. Commun. **180**, 2622 (2009).
[24] D. Reith, Ph.D. thesis, Vienna University, 2011.
[25] See Supplemental Material at http://link.aps.org/supplemental/10.1103/PhysRevB.102.075117 for more details regarding composition, microstructure, and morphology.
[26] I. Knapp, B. Budinska, D. Milosavljevic, P. Heinrich, S. Khmelevskyi, R. Moser, R. Podloucky, P. Prenninger, and E. Bauer, Phys. Rev. B **96**, 045204 (2017).
[27] M. Kato, Y. Nishino, S. Asano, and S. Ohara, J. Jpn. Inst. Met. **62**, 669 (1998).
[28] E. J. Skoug, C. Zhou, Y. Pei, and D. T. Morelli, J. Electron. Mater. **38**, 1221 (2009).
[29] M. Mikami, M. Mizoshiri, K. Ozaki, H. Takazawa, A. Yamamoto, Y. Terazawa, and T. Takeuchi, J. Electron. Mater. **43**, 1922 (2014).
[30] H. J. Goldsmid and J. W. Sharp, J. Electron. Mater. **28**, 869 (1999).
[31] Z. M. Gibbs, H.-S. Kim, H. Wang, and G. J. Snyder, Appl. Phys. Lett. **106**, 022112 (2015).
[32] Y. Zhang, E. Skoug, J. Cain, V. Ozoliņš, D. Morelli, and C. Wolverton, Phys. Rev. B **85**, 054306 (2012).

[33] R. Moser, Ph.D. thesis, Vienna University of Technology, 2016.
[34] O. L. Anderson, J. Phys. Chem. Solids **24**, 909 (1963).
[35] J. Callaway, Phys. Rev. **113**, 1046 (1959).
[36] Z. Zhou, C. Uher, A. Jewell, and T. Caillat, Phys. Rev. B **71**, 235209 (2005).
[37] A. Pope, B. Zawilski, and T. Tritt, Cryogenics **41**, 725 (2001).
[38] B. Abeles, Phys. Rev. **131**, 1906 (1963).
[39] J. Yang, G. P. Meisner, and L. Chen, Appl. Phys. Lett. **85**, 1140 (2004).
[40] S. V. Ovsyannikov, V. V. Shchennikov, G. V. Vorontsov, A. Y. Manakov, A. Y. Likhacheva, and V. A. Kulbachinskii, J. Appl. Phys. **104**, 053713 (2008).